ACS Catalysis

Open Access

This article is licensed under CC-BY 4.0

pubs.acs.org/acscatalysis

Research Article

Alkali Hydride-Iron Oxide-Nanocomposites as Catalysts for Low-Temperature Ammonia Synthesis

Juliette C. Verschoor, Fabian J. Mohammad, Masoud Lazemi, Shusaku Hayama, Nitya Ramanan, Frank M. F. de Groot, Petra E. de Jongh, and Peter Ngene*

Cite This: https://doi.org/10.1021/acscatal.6c02968

Read Online

ACCESS | Metrics & More | Article Recommendations | Supporting Information

ABSTRACT: Fertilizers derived from ammonia (NH_3) play a vital role in global food production, and ammonia is also emerging as a carbon-free fuel or hydrogen carrier. To facilitate the use of ammonia as an energy carrier, there is a need to develop catalysts that enable ammonia production under milder conditions than the current Haber–Bosch process. Industrially, high temperatures and pressures (>450 °C, >100 bar) are required, partly due to the need to operate at conditions where the iron oxide (Fe_2O_3) catalysts are reduced to the active Fe phase. Herein, we show that intimate contact between Fe_2O_3 nanoclusters and alkali metal hydrides (LiH, NaH, and KH), arising from their co-confinement in nanoporous carbon, leads to high ammonia production under mild conditions (~250 °C and 10 bar), without prior reduction of the Fe_2O_3. The alkali metal hydrides show profound differences in catalytic activity due to the differences in their interaction/reactivity with Fe_2O_3 nanoparticles, as well as activation of N_2. These results show that co-nanoconfinement of metal hydrides and transition metal oxides is a promising approach toward developing catalysts for low-temperature ammonia synthesis.

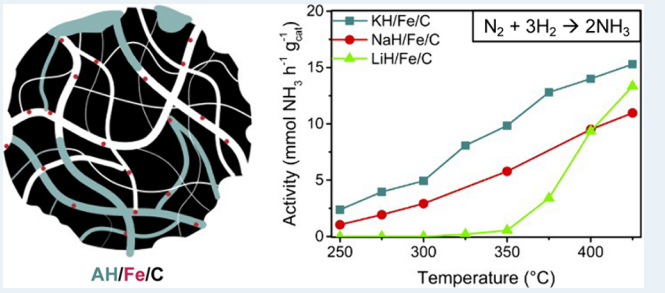

KEYWORDS: *ammonia synthesis, nanocomposite, moderate conditions, promotion, alkali hydride, carbon support*

1. INTRODUCTION

Ammonia is amongst the most produced chemicals used in the production of synthetic fertilizers for agriculture.[1,2] It also receives great interest as an energy carrier due to its high hydrogen content (17 wt% H), ease of transportation, and stability over time.[3–5] However, future implementations as a sustainable fuel should also coincide with improvements in the efficiency and carbon footprint of ammonia synthesis. While ammonia synthesis from the elements is exothermic and hence favored at low temperatures, industrially, the reaction is performed at high temperature and pressure (>450 °C, 100 bar). The reason is the high kinetic barriers associated with the activation and transformation of the strong triple-covalent dinitrogen bond.[6–8] The contribution of ammonia production to global energy consumption and CO_2 emissions, including prior hydrogen synthesis, amounts to 1–2%.[9–11] Although some aspects of the current industrial synthesis route benefit from high pressure, the development of efficient and robust catalysts that can facilitate this reaction under milder reaction conditions is highly desirable. The mild reaction conditions are especially suitable for coupling intermittent and low hydrogen pressure sources from solar and wind farms.

The most used ammonia synthesis catalysts are based on transition metals (TM). The catalytic activity of these TM-based catalysts exhibits a volcano-shaped dependence on the nitrogen adsorption energy.[12] Industrially, the reaction can be carried out at 400–500 °C and 100–300 bar using either iron (Fe) or ruthenium (Ru) promoted with alkali metal oxides. Although Ru-based catalysts of the KAAP process exhibit higher intrinsic activity, high costs limit their large-scale use. In addition, Ru suffers from hydrogen poisoning at high pressure. Therefore, currently, Fe-based catalysts are the most commonly used in industry.

Great efforts have been devoted in recent years to realizing efficient NH_3 synthesis under mild conditions (≤400 °C and ≤20 bar). Most of these efforts have focused on the addition of alkali metal (AM) or alkaline-earth metal (AEM) oxides (K_2O, Cs_2O, BaO)[9,13–15] and electrides[16–18] as promoters. These promoters have been shown to enhance the catalytic activity by donating electrons to both the Fe metal and N_2. Breaking the dinitrogen bond is generally the rate-limiting step, and electron donation facilitates N_2 activation on the Fe.

Received: April 14, 2026
Revised: July 2, 2026
Accepted: July 6, 2026

Downloaded from http://pubs.acs.org/accacs/article-pdf/doi/10.1021/acscatal.6c02968/66127963/cs-2026-029683.pdf by guest on 27 July 2026

© XXXX The Authors. Published by American Chemical Society

Promoters, by definition, are expected to exhibit limited to no activity on their own, but improve the catalytic performance of already catalytically active phases. The use of promoters in the design of a more energy-efficient catalyst is limited by the "scaling relation". This scaling relation relates the adsorption strength of N_2 on TMs to those of the NH_x intermediates.[19]

Recently, alkali- and alkaline earth- metal hydrides (such as LiH, CaH_2, and BaH_2), as well as aluminum hydride, have emerged as both electronic promoters and additional active sites.[20−22] These hydride promoters offer a pathway to circumvent the scaling relations via their dual-site mechanism, while also providing strong electron donation.[21,23,24] Combining these hydrides with Fe (also other transition metals such as Mn, Co, Ni, and V) lowers the apparent activation energies for NH_3 synthesis.[23,24] The effects have been related to the ability of the metal hydride to store hydrogen reversibly, in combination with the high electron-donating properties of the hydride ion (H^-). Hydrides combine electronic promotion and reversible hydrogen storage properties, setting them apart from classical oxide-based promoters. Nanoconfinement of these metal hydrides within a nanoporous carbon support has been shown to significantly improve their catalytic activity and hydrogen release kinetics in hydrogen storage applications.[22,25] This is attributed to the high dispersion, proximity, and thereby interaction with the carbon matrix.

So far, most efforts to improve catalytic activity under mild conditions have focused on pure Fe, either as nanoparticles or single-atom catalysts.[9,26−28] However, industrial catalysts typically contain about 98% iron oxide (Fe_2O_3) mixed with alkali metal or alkaline-earth metal oxide promoters, and are supported on alumina (Al_2O_3).[29,30] The catalysts are prepared by heating a mixture of these precursors to the molten state at about 1600 °C. Even after this treatment, the commercial catalysts still contain a significant amount of Fe_yO_x phase; as a result, a pre-reduction treatment is conducted around 500 °C under high hydrogen pressure before the actual catalysis.

Herein, we demonstrate that co-confinement of oxidic iron (Fe_yO_x) nanoclusters and alkali metal hydrides in nanoporous carbon leads to high ammonia activity under mild conditions (~250 °C and 10 bar), even without prior reduction of the Fe_yO_x at elevated temperatures. The high activity is due to close contact and interaction between the nanoconfined Fe_yO_x and the alkali metal hydrides. The close contact facilitates in-situ reduction of the Fe_yO_x, and the activation and hydrogenation of N_2 to NH_3. Using well-defined carbon-supported Fe_yO_x nanoparticles in combination with three alkali metal hydrides (KH, NaH, and LiH), we show that the catalytic activity is strongly dependent on the interaction/reactivity of the alkali metal hydrides with Fe_yO_x nanoparticles, as well as with N_2 and H_2. This work paves the way for developing active NH_3 synthesis catalysts that overcome the need for reduction at elevated temperatures and pressures.

2. EXPERIMENTAL SECTION

2.1. Synthesis

2.1.1. Materials. All chemicals were stored in an Ar-filled glovebox (O_2 < 1 ppm, H_2O < 1 ppm). Graphene nanoplatelets (GNP-500, XG Sciences, grade C, specific surface area of 500 m^2 g^{-1}) was used as graphitic carbon support. GNP-500 contains ~0.13 at% of N and ~3.73 at% of O based on XPS analysis.[31] Iron nitrate nonahydrate ($Fe(NO_3)_3(H_2O)_9$, Sigma Aldrich, ≥97.4%) and nitric acid (HNO_3, Merck, 65%) were used as received to prepare the aqueous iron nitrate solution for incipient wetness impregnation. Potassium hydride (KH), Sodium hydride (NaH), and Lithium hydride (LiH) were purchased from Sigma-Aldrich. The alkali hydrides (AH) were delivered under an inert atmosphere and in mineral oil. The mineral oil was washed off with hexane, which was removed by drying under an inert atmosphere. Magnesium oxide nanopowder was obtained from Strem Chemicals and Ru (III) acetylacetonate (99.5%) from Sigma-Aldrich.

2.1.2. Catalyst Synthesis. Carbon supported iron (Fe/C) was first made via incipient wetness impregnation of an acidified (pH ~1) aqueous iron nitrate ($Fe(NO_3)_3(H_2O)_9$) solution. The carbon support was first dried in a round-bottom flask for 120 min at 170 °C, while stirring under dynamic vacuum to evacuate water and air from the pores. This was followed by impregnation with the aqueous $Fe(NO_3)_3(H_2O)_9$ solution under dynamic vacuum to obtain $Fe(NO_3)_3$/C. For catalytic testing, an appropriate amount of aqueous $Fe(NO_3)_3(H_2O)_9$ solution was impregnated to obtain a final Fe weight loading of 1 wt%, which resulted in a fine dispersion of small Fe nanoparticles, thereby improving the contact between the different phases. The $Fe(NO_3)_3$/C was subjected to heat treatment (350 °C for 1.5 h under N_2 flow to obtain FeO/C followed by reduction treatment (350 °C for 1.5 h under H_2/N_2 flow) to obtain Fe/C. The F/C was then stored in the glovebox until further use. The Fe/C + alkali hydride catalysts were prepared by mixing the carbon-supported Fe nanoparticles and the alkali metal hydride (LiH, NaH, KH). The components were transferred to a mortar and ground for 5 min, ensuring a homogeneous mixture. The mixture was transferred to a quartz crucible and heated to 400 °C under Ar flow (heat treatment), followed by an isothermal hold for 2 h. This step leads to partial decomposition and infiltration of the alkali hydride into the graphitic carbon. This catalyst (AH/Fe/C) was cooled under Ar flow and then transferred to the Ar glovebox, where it was kept without exposure to oxygen or moisture. We aimed to load the same amount of mole AH per gram of catalyst. Due to the large differences in molar weight, the weight loadings of AH were adjusted as shown in Table 1.

The 5 wt% Ru/MgO reference catalyst was prepared via wet impregnation of MgO with an acetone solution of ruthenium acetylacetonate ($Ru(acac)_3$) precursor. After drying in air overnight, the catalyst was a light red/pink-ish powder. The catalyst powder was then reduced under a 10% H_2/N_2 flow at a ramping of 2 °C min^{-1} to 400 °C, where it was held for 2 h. This treatment yielded a grey powder and was then transferred to the glovebox until further use.

2.1.3. N_2 and H_2 Treatments. The fresh catalyst (~200 mg, AH/Fe/C) was loaded into a quartz sample holder with a lid and placed inside a stainless steel autoclave. For the N_2 treatment, an initial pressure of 20 bar N_2 was applied at room temperature, after which the sample was heated to 285 °C for 10 h. For the H_2 treatment, an initial pressure of 20 bar H_2 was applied at room temperature, after which the sample was heated to 285 °C for 2 h. After cooling, the remaining gas was vented, and the autoclave was transported to the Ar glovebox without exposure to air. The treated sample was removed from the autoclave and stored in the Ar glovebox.

2.2. Characterization

2.2.1. X-ray Diffraction. The presence of crystallographic phases and graphitic properties of the graphitic carbon support of the composites were measured with powder X-ray diffraction (XRD) on a Malvern Panalytical Empyrean powder X-ray diffractometer using a Molybdenum source (Mo $K_{\alpha1,2}$ radiation, λ = 0.7093 Å) at 60 kV

Table 1. Alkali Hydride and Catalyst Properties

4.17 mmol g_{cat}^{-1}	M_w (g mol^{-1})	wt%	at%	AH:Fe (1 wt% Fe)
LiH	7.95	3.31	4.92	22:1
NaH	23.998	10.00	5.26	23:1
KH	40.1062	16.71	5.66	24:1

Downloaded from http://pubs.acs.org/accacs/article-pdf/doi/10.1021/acscatal.6c02968/66127963/cs-2026-029683.pdf by guest on 27 July 2026

https://doi.org/10.1021/acscatal.6c02968
ACS Catal. XXXX, XXX, XXX−XXX

and 40 mA. Diffractograms were measured at room temperature from 5° to 45° 2θ, with 0.014° step increments, in an argon-filled and sealed sample holder.

2.2.2. Temperature–Programmed Desorption. Temperature–programmed desorption (TPD) was performed on a Micromeritics AutoChem II 2920 apparatus. The measurements were carried out under argon flow to detect the hydrogen release from the samples, which was quantified using a thermal conductivity detector (TCD) signal in combination with an H_2/Ar calibration. If desired, the outgoing gas was also analyzed using a mass spectrometer (MS) from Hidden Analytical equipped with the QGA Professional software package. These TPD measurements enabled the determination of the hydrogen content in the nanocomposite before catalysis, as well as changes in decomposition temperature of the AH nanocomposites compared to the bulk AH.

2.2.3. Temperature–Programmed Reduction. Temperature–programmed reduction (TPR) was performed on a Micromeritics AutoChem II 2920 apparatus. The measurements were carried out under a 5% H_2/Ar flow to monitor the hydrogen uptake from the samples. They were quantified based on the thermal conductivity detector (TCD) signal in combination with a H_2/Ar calibration. The outgoing gas was also analyzed using a mass spectrometer (MS) from Hidden Analytical, equipped with the QGA Professional software package. To study the reduction of the Fe_yO_x to Fe, 150 mg of FeO/C catalyst was dried at 120 °C under Ar flow for 1 h. The sample was cooled down to room temperature before switching to 5% H_2/Ar flow of 25 mL min^{-1} at 5 °C min^{-1} up to 800 °C. For the hydrogenation of nitrogen-treated samples, 70 mg of N_2-AH/Fe/C was loaded and heated to 425 °C at 5 °C min^{-1}, under 5% H_2/Ar flow of 25 mL min^{-1}.

2.2.4. Nitrogen Physisorption. Nitrogen physisorption was conducted at 77 K on a TriStar II Plus gas-volumetric instrument (Micromeritics). The BET surface area was based on the fitting of the experimental data with a Brunauer-Emmett-Teller isotherm, in accordance with the Rouquerol criteria. The pore volume of the different components was determined from the volume of absorbed N_2 at $p/p_0 = 0.995$.

2.2.5. HAADF-STEM-EDX. Scanning Tunnelling Electron Microscopy (STEM) was performed using a TALOS F200X microscope of ThermoFischer, operating at 200 kV. Semi-quantitative elemental analysis and chemical mapping were performed using energy-dispersive X-ray (EDX) spectrometry. The catalysts were dispersed as a dry powder onto a Cu sample grid coated with holey carbon. At least 150 iron nanoparticles were manually counted per sample on at least 10 different locations using ImageJ software. Both the number-averaged particle diameter (d_n) and surface-averaged particle diameter (d_s) of the iron particles, including their standard deviations, were calculated.[32]

2.2.6. HERFD-XANES. Fe K-edge high-energy-resolution fluorescence detection with X-ray adsorption near edge structure (HERFD-XANES) spectra were collected at the I20-Scanning beamline at Diamond Light Source (DLS), using the four-bounce Si(111) monochromator and the XES spectrometer equipped with seven spherically bent Ge(440) analyzers to measure the Fe K_α emission line.[33] The high resolution of HERFD-XANES enables us to study the local symmetry of iron and probe the local environment.[34−37] Fe Kα-XANES spectra were collected in one session over the incident range of 7000–7300 eV with the spectrometer fixed at the peak of the Fe K_α line. X-ray energies were calibrated by reference to the absorption of a Fe standard metal foil. The beam spot size was 300 μm × 400 μm. Beam damage was assessed at the pre-edge (7114.8 eV) and at the white line (7132.7 eV), as these areas are sensitive to the structure and oxidation state of the iron. Based on the signal at these energies, the attenuation was adjusted, resulting in the use of a 1 mm thickness carbon filter. With proper attenuation, we did not observe any dose-dependent spectral changes. The data processing was done with Athena data processing software.[38] The background in each post-edge and each pre-edge was fit with a linear line (normalization order 2).

The samples were pressed into pellets, affixed to a sample holder with carbon tape, and sealed in an aluminized Mylar bag, all within an argon glovebox. This aluminized Mylar bag was sealed in the glovebox to ensure measurements under an inert atmosphere. Fe-foil, $FeSO_4{\cdot}7H_2O$, and $Fe(NO_3)_3{\cdot}9H_2O$ aqueous solutions (50 mM) were used as references for our standard linear combination fitting, based on earlier work by Yao et al.[39]

2.2.7. Catalytic Testing. All catalytic tests were carried out using a home-built, fixed-bed reactor, catalytic testing setup as described in an earlier paper.[22] The catalyst, typically 200 mg, was loaded into a quartz tube (inner diameter 8 mm and outer diameter 11 mm). The catalytic tests were performed under a continuous flow of N_2:H_2 (1:3, purity > 99.9999%). The temperature was increased with a ramp rate of 5 °C min^{-1}, and measurements were conducted during an isothermal hold of 20 min. The pressure was kept at 10 bar, and the flow rate varied between 20 and 100 mL min^{-1}. The gas outlet was connected to a trap containing diluted sulfuric acid, where the generation of NH_4^+ resulted in a change in conductivity. Calibrations with 1% NH_3/He (purity > 99.9999%) gave a conversion factor of 0.687 μmol of NH_3 formed per μS cm^{-1}.

3. RESULTS—FE/C SYNTHESIS

Figure 1 illustrates the general schematic for the preparation of our catalyst via the melt infiltration of alkali metal hydride onto a porous carbon support with iron nanoparticles (AH/Fe/C). We begin by synthesizing the carbon-supported Fe_yO_x nanoparticles. The catalysts were made through impregnation of a carbon support with iron nitrate solution ($Fe(NO_3)_3$), followed by thermal decomposition of the $Fe(NO_3)_3$ to form iron oxide (Fe_2O_3) at 350 °C under N_2 and/or a mixture of 5% H_2/N_2 (Figure 1). As will be discussed in the next section, the thermal decomposition under 5% H_2/N_2 does not reduce Fe_2O_3 to metallic iron (Fe) but facilitates a high dispersion of Fe_2O_3 on the carbon. Subsequently, the carbon-supported iron nanoparticles (referred to as Fe/C from here) were thoroughly mixed with the alkali hydride (AH) using a pestle and mortar. The mixture was heated to 400 °C under argon. This step led to partial decomposition of the metal hydride and infiltration of the molten metal phase into the carbon pores to form intimate contact with the Fe_2O_3 nanoparticles.

TPR-MS was used to investigate the conditions required to reduce Fe oxide under hydrogen. Figure S1 shows that the onset of hydrogen consumption occurs at 200 °C, with a peak around 400 °C. The signal at 200 °C could indicate the beginning of Fe oxide (Fe_2O_3) reduction, most likely to an

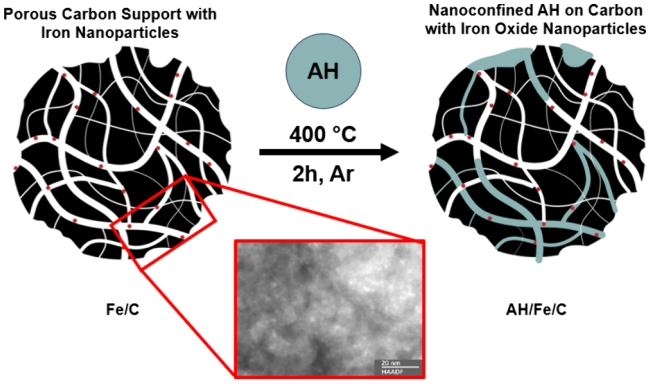

Figure 1. Schematic illustration of heat treatment with the alkali hydride is performed to induce melt infiltration. Adapted from reference 40 with permission. Copyright 2016, Elsevier.

https://doi.org/10.1021/acscatal.6c02968
ACS Catal. XXXX, XXX, XXX−XXX

Downloaded from http://pubs.acs.org/accacs/article-pdf/doi/10.1021/acscatal.6c02968/66127963/cs-2026-029683.pdf by guest on 27 July 2026

intermediate state such as Fe_3O_4 or FeO. However, the formation of CO and CO_2, as seen from the TPR-MS measurements (Figure S2), shows that other reactions are occurring. This is likely the removal of the carboxylic surface groups on the carbon support, as observed by Visser et al.[32] The second hydrogen peak at 650 °C, observed in both the MS and TCD results, overlaps exactly with methane formation, which begins around 500 °C and peaks around 600 °C. Based on these observations, the thermal treatment to 350 °C under 5% H_2/N_2 does not reduce the Fe_2O_3 but rather aids the removal of the carbon surface groups, without methanation of the carbon.

The particle size of the Fe_2O_3 nanoparticles was determined using HAADF-TEM, while the distribution and presence of Fe_2O_3 were confirmed via STEM-EDX (Figure S3). The average particle size was 2 nm, both numerical and Sauter mean (Figure S4). Note that such small particles and a fine distribution are desired for enhanced interface/interaction between Fe_yO_x and AH. Due to the small particle size and low weight-loading of the Fe_yO_x, XRD could not give any meaningful insight into the catalyst's structure; hence, HERFD-XANES was used to determine the Fe phase. Figure S5 compares the as-prepared Fe/C and Fe_yO_x reference materials (Fe foil, FeO, and Fe_2O_3 for Fe^0, Fe^{2+}, and Fe^{3+}, respectively). The figure indicates the presence of Fe^{3+}, but due to the incomplete match between the reference materials and the Fe/C catalyst, the linear combination fitting was challenging. Specifically, the edge jump of Fe/C appears to indicate a similar or even slightly higher oxidation state compared to the Fe_2O_3 reference. Although uncertain of the exact origins of this discrepancy, Yao et al. found that for iron nanoparticles, better linear combination fits are obtained using dissolved Fe salts.[39] We found that using these Fe salts for linear combination fitting accommodated the effects of nanosizing, resulting in fits with $R^2 = 0.9875$ on average. These LCF results are summarized in Table S1. The carbon-supported nanoparticles prior to the addition of AH could be fit with $R^2 = 0.9982$ using these references, which gave a Fe^{3+} concentration of 95%.

These results prove that our preparation route led to well-defined and highly dispersed Fe_2O_3 nanoparticles on the carbon supports. The Fe/C (precisely Fe_2O_3/C) was mixed with an appropriate amount of alkali metal hydride (LiH, KH, or NaH) and heated to 400 °C under argon. The XRD and HERFD-XANES of these nanocomposites are displayed in Figure 2. As described earlier, this treatment results in partial or complete decomposition of the metal hydride, followed by the infiltration of the molten metal phase into the carbon pores to form the active catalyst. This technique (melt infiltration) has been used extensively for the synthesis of nanoconfined metal hydrides for reversible hydrogen storage applications.[41,42]

The bare alkali hydride and carbon support were measured independently, and are displayed in Figure 2a. The carbon support shows the typical reflections for graphitic carbon, and for the AH + Fe/C physical mixtures, the KH and NaH reflections are clearly observed (Figure S6). The subsequent heat treatment results in (partial) dehydrogenation of the alkali hydrides. The (partial) dehydrogenation of KH facilitates the formation of potassium hydride-graphite intercalated compounds (KH-GIC, Figure 2c). The absence of AH reflections (12°–17°) after the heat treatment indicates that the alkali metal or partially decomposed hydride is highly dispersed on the carbon and lacks long-range crystallinity upon nanoconfinement.[41,42] The changes in nanocomposite reflections due to heat treatment (and later after catalysis) are more apparent when compared to their physical mixtures (Figure S6). Intercalation of KH has been reported when graphitic carbon materials were used to prepare KH/C nanocomposites (KH-GIC).[22]

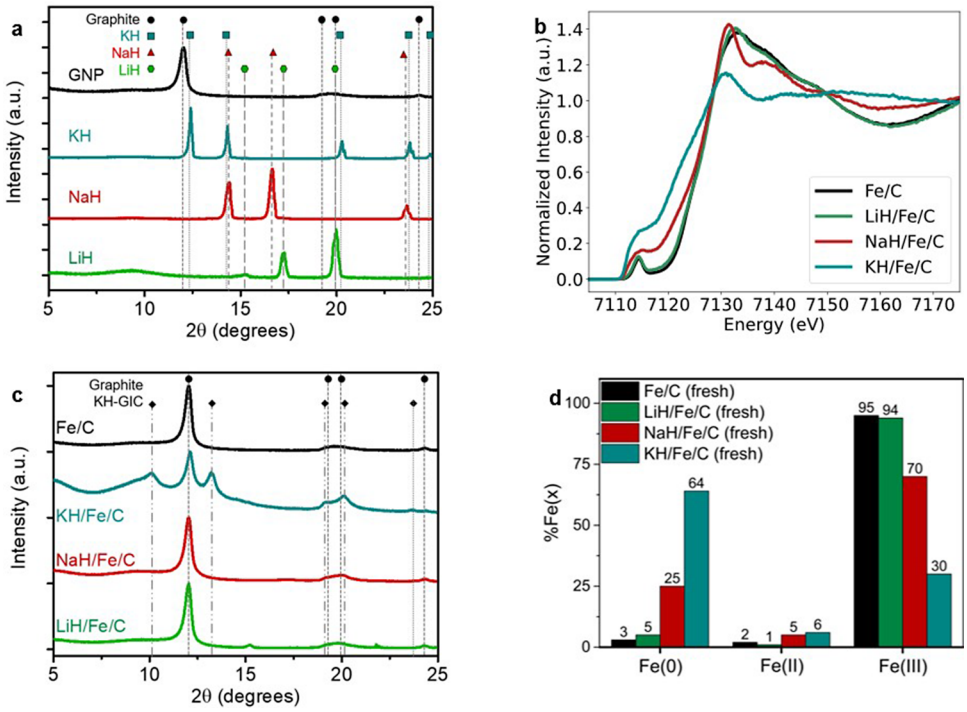

Figure 2. (a) XRDs of the bare carbon and alkali hydride materials, (b) the Fe K-edge HERFD-XANES spectra, (c) XRDs, and (d) the linear-combination fitting results of the fresh AH/Fe/C catalysts and the Fe/C reference catalyst.

Downloaded from http://pubs.acs.org/accacs/article-pdf/doi/10.1021/acscatal.6c02968/66127963/cs-2026-029683.pdf by guest on 27 July 2026

https://doi.org/10.1021/acscatal.6c02968
ACS Catal. XXXX, XXX, XXX–XXX

The formed KH-GIC phase can catalyze ammonia synthesis at moderate temperatures, even without a transition metal.[22] In our case, there is indeed a shift in the carbon reflections of KH/Fe/C, but some of the main reflections of the graphitic C are still present, indicating that some of the graphite has not been intercalated with KH. The difference in the degree of intercalation compared to the previous study, in which all the C was intercalated, is likely due to the difference in the properties of the carbon scaffolds, which are known to influence ion intercalation. On the other hand, the slight shift in the C peaks indicates a limited intercalation of KH, but is negligible for the NaH and LiH-based nanocomposite, suggesting that Na and Li do not readily intercalate into this carbon material under the experimental conditions.

Nitrogen physisorption (Figure S7 and Table S2) was used to demonstrate confinement of the AHs in the carbon pores. The surface area and pore size distribution of the pure carbon support and the FeO_x/C are quite similar. The majority of the pores are around 2 nm, with a continuous distribution up to 100 nm. Although the AH/Fe/C nanocomposites maintain the porous structure of the carbon, they show a significant decrease in the pore volume between 2 and 40 nm, suggesting that the AH is confined in the pores. The pore volume losses exceed the total volume of alkali metal (hydride) added, which suggests a significant degree of pore blocking in both micro- and mesopore regimes. This pore blocking and the consequent loss of (micro)pore volume is much more prominent for KH/Fe/C and NaH/Fe/C, where 0.29 and 0.31 $cm^3\ g^{-1}$ of pore volume was lost compared to the 0.19 and 0.10 $cm^3\ g^{-1}$ of alkali metal (hydride) which was added. The limited pore volume loss of LiH/Fe/C (0.09 $cm^3\ g^{-1}$) is attributed to the fact that most of the LiH has not decomposed during the synthesis and therefore has not fully melted to infiltrate the pores.

STEM-EDX measurements were performed to visualize the distribution of the different components in the fresh catalysts (after melt infiltration) and assess the proximity between iron and the alkali metals potassium and sodium. As can be seen in Figures S8–S11, the iron nanoparticles are homogeneously distributed throughout the carbon supports. The alkali metals are detected in three distinct configurations: (i) finely distributed throughout the support, (ii) on the external surface of the carbon particles, and (iii) as agglomerates throughout the carbon support. These measurements confirm the intimate contact and co-confinement within the porous carbon support.

To study the effect of the AH addition on the Fe_2O_3, the oxidation state and local environment of Fe in the AH/Fe/C catalysts were analyzed using HERFD-XANES (Figure 2b). Without the addition of AH, the FeO/C spectrum and %Fe^0 do not change significantly even after the reduction treatment (5% H_2/N_2, 1 bar, 350 °C) and subsequent catalytic testing (75% H_2/N_2, 10 bar, 250–425 °C) (Figure S12, Table S1). The absence of peaks in the post-edge region suggests low long-range order, which correlates with the small individual nanoparticles observed with TEM.[37] Figure 2b shows that the addition of the AH leads to profound changes in the Fe edge spectra, as indicated by the change in shape of the pre-edge and shift of the edge jump to lower energies. The edge shift to lower energies is most prominent for KH/Fe/C and is characteristic of a change in oxidation state, namely the (partial) reduction of Fe_2O_3. The subsequent loss of pre-edge features due to increased Fe-Fe contribution in this region limits the probing of the local coordination environment.[37] However, this environment can still be probed using the post-edge features, specifically in the 7135 to 7145 eV range.[39,43–45] Interestingly, the effect of the AH addition differs largely across the different AHs. While LiH leads to slight changes compared to the Fe/C starting material, the NaH/Fe/C and KH/Fe/C samples show a larger shift to more reduced iron. The relative fractions of Fe^{3+}, Fe^{2+}, and Fe^0 in the nanocomposites were determined based on linear combination fitting using the XANES spectra from $Fe(NO_3)_3$, $FeSO_4$, and Fe foil, respectively (Figure S13). The Fe foil was stored and measured under an argon atmosphere to avoid partial oxidation. The linear combination fits of the fresh catalysts are shown in Figures S14–S17 and the results are summarized in Figure 2d and Table S1. These results show that NaH/Fe/C and KH/Fe/C have an Fe^0 content of about 5 and 12 times higher than that of LiH/Fe/C. These observations suggest that the addition of the AH facilitates the reduction of Fe_2O_3 nanoparticles under these mild conditions (400 °C, Ar) more than a hydrogen atmosphere does. The presence of AH likely promotes reduction by increasing the electron density on the iron oxide.

It should be noted that all catalysts were prepared with the same AH molar loading (4.17 mmol AH g_{cat}^{-1}). This results in a significant difference in weight loading due to the difference in molecular weight. LiH is thermally the most stable amongst the AH used and is therefore expected to be less reactive and/or mobile at 400 °C. The stability of LiH could limit its ability to facilitate the reduction of Fe_2O_3 under these mild conditions. To assess whether the lower degree of reduction observed for LiH/Fe/C originates from the intrinsic properties or accessibility of LiH, the weight loading was increased to 10 wt % (12.62 mmol AH g_{cat}^{-1}). Indeed, increasing the wt% loading of LiH led to a higher degree of Fe_2O_3 reduction, from 5 to 58 %Fe^0 (Table S1).

This result indicates that although LiH is the most thermally stable of the AHs, it is capable of interacting with and facilitating the reduction of Fe_2O_3. Since the LiH/Fe/C has a similar molar ratio of AH to Fe_2O_3, compared to the NaH and KH containing samples, the lower degree of reduction (amount of Fe^0) compared to the NaH- and KH-containing samples is likely due to other factors, such as the distribution of LiH on the Fe/C, or differences in reactivity. Indeed, the HERFD-XANES suggest additional effects (Figure S18). These aspects will be addressed more extensively in the following sections. In summary, the results from the TPR-MS, STEM-EDX, and HERFD-XANES demonstrate that the as-prepared catalysts consist of well-dispersed Fe_2O_3 nanoparticles that are partially reduced by the presence of the alkali hydride. Note that performing melt infiltration of AHs without fully reducing the Fe_2O_3 nanoparticles (at higher temperatures and hydrogen pressure) ensures retention of the fine dispersion and distribution of the Fe_2O_3 on the carbon.

4. RESULTS—CATALYTIC ACTIVITIES OF AH/FE/C

The AH/Fe/C catalysts were stored in a glovebox after synthesis and then placed in an airtight fixed-bed reactor to evaluate the ammonia synthesis performance. A 1:3 mixture of N_2 and H_2 was flown through the catalyst bed, and the outlet gas was bubbled through a sulfuric acid solution, where a calibrated conductivity meter quantitatively measured the NH_3 production. Figure 3a displays the production of NH_3 over the temperature range 250–425 °C. While the Fe/C (Fe_2O_3/C) and AH/C

Downloaded from http://pubs.acs.org/accacs/article-pdf/doi/10.1021/acscatal.6c02968/66127963/cs-2026-029683.pdf by guest on 27 July 2026

https://doi.org/10.1021/acscatal.6c02968
ACS Catal. XXXX, XXX, XXX–XXX

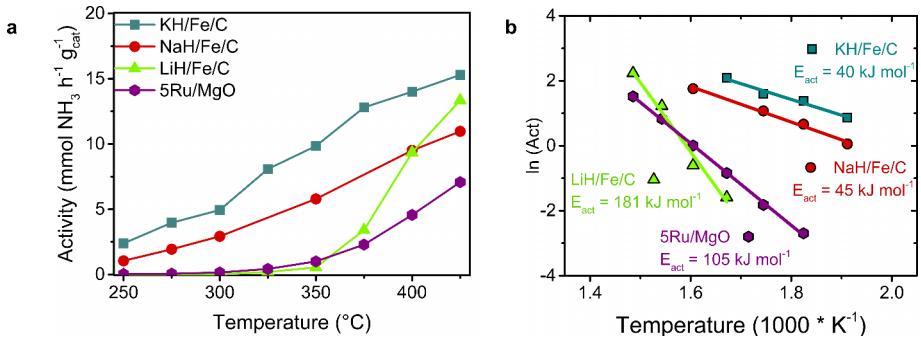

Figure 3. (a) Temperature dependences of the activities of different AH/Fe/C catalysts (AH = LiH, NaH, and KH) and the reference 5Ru/MgO catalyst for NH_3 synthesis. Reaction conditions: 10 bar, 250–425 °C, and 18,000 mL g_{cat}^{-1} h^{-1}. (b) Arrhenius plots of the AH/Fe/C catalysts and the reference 5Ru/MgO catalyst under reaction conditions.

exhibit limited NH_3 production at 400 °C (Figure S19), AH/Fe/C nanocomposites show significantly higher ammonia production, which increases with increasing temperatures. Note that to ensure a fair comparison, all the catalysts contain the same molar loading of AH (4.17 mmol AH g_{cat}^{-1}). Ru is generally considered the most active transition metal for ammonia synthesis. Therefore, the catalytic activity of unpromoted 5 wt % Ru/MgO was compared to those of the AH/Fe/C nanocomposites. Clearly, the AH/Fe/C nanocomposites show superior catalytic performance under these mild conditions.

At lower temperatures, the catalyst activity follows the trend KH > NaH > LiH; however, at higher temperatures (≥425 °C), the trend reverses to KH > LiH > NaH. Based on the HERFD-XANES of the fresh catalysts in (Table S1), LiH/Fe/C has the lowest %Fe^0 and is the only catalyst that shows a delayed onset in catalytic activity. The apparent activation energies (E_{act}) of NH_3 synthesis over these AH/Fe/C nanocomposites were derived from the Arrhenius plots (Table S2 and Figure 3b), and span a broad range. The E_{act} values of KH/Fe/C and NaH/Fe/C (40 and 45 kJ mol^{-1}, respectively) are comparable to those reported for similar other AH-transition metal systems (46–64 kJ mol^{-1})[20,23,24] and much lower than the E_{act} of 5Ru/MgO (105 kJ mol^{-1}). The similar activation energies for the KH and NaH catalysts do not correlate with their average iron oxidation state (%Fe^0, Table S1). This suggests that the electronic promotion effect of KH and NaH is not limited to the Fe_yO_x reduction, but also extends to the N_2 activation on Fe. These values strongly deviate from the LiH/Fe/C catalyst (181 kJ mol^{-1}).

To gain insight into the state of the catalyst after reaction and during cooling, the spent catalysts were characterized. The XRD diffractograms of the spent catalysts in Figure S6 did not show any reflections from the AHs, indicating a further loss of crystallinity of the AHs during catalysis. No significant change could be seen in the HERFD-XANES spectra of the Fe_yO_x/C during catalysis (Figure S12). This is a strong indication that the oxidation state of Fe is hardly affected under these mild reaction conditions, but the presence of the AHs greatly facilitates the reduction of Fe_2O_3.

Similar to the Fe_2O_3/C, the HERFD-XANES spectra of NaH/Fe/C and KH/Fe/C showed only minor changes after catalysis, suggesting no significant changes in the oxidation state of the Fe (Figure S20). However, the LiH/Fe/C shows a remarkable increase in %Fe^0 when comparing the spent and fresh catalysts (Figure 4a, b and Table S1). Interestingly, NaH/Fe/C and KH/Fe/C maintained their catalytic activity during cooling (Figure 4c), while LiH/Fe/C showed much higher ammonia synthesis activity over a larger temperature range during cooling, compared to the heating ramp. Thus, the increased activity of LiH/Fe/C during cooling coincides with an increase in %Fe^0. Based on the changes in temperature-dependent activity and %Fe^0, LiH/Fe/C has undergone a secondary reduction during catalysis. Additionally, the E_{act} of LiH/Fe/C during cooling is in the

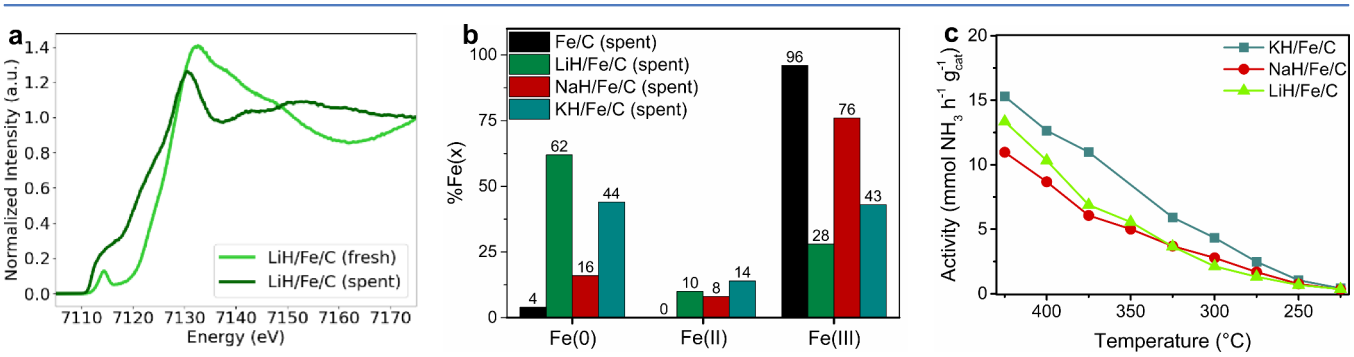

Figure 4. (a) The Fe K-edge HERFD-XANES spectra of the fresh and spent LiH/Fe/C catalysts, (b) the linear-combination fitting results of the spent AH/Fe/C catalysts, and (c) NH_3 synthesis catalysed by AH/Fe/C. Temperature dependence of the NH_3 production rate of AH/Fe/C during cooling. Reaction conditions: 10 bar, 425–225 °C, and 18,000 mL g_{cat}^{-1} h^{-1}.

https://doi.org/10.1021/acscatal.6c02968
ACS Catal. XXXX, XXX, XXX–XXX

Downloaded from http://pubs.acs.org/accacs/article-pdf/doi/10.1021/acscatal.6c02968/66127963/cs-2026-029683.pdf by guest on 27 July 2026

same range as the other catalysts (53–68 kJ mol^{-1}, Figure S21). These activities during cooling are similar to other LiH-TM catalysts, 2–5 mmol NH_3 g^{-1} h^{-1}, and higher than NaH-TM and KH-TM catalysts at 300 °C and 10 bar.[20,24,46]

Increasing the amount of LiH resulted in an increase in the concentration of Fe^0 to 58% after catalyst preparation, comparable to that of KH/Fe/C (64%, Table S1). Despite this similar %Fe^0, the high-loading LiH/Fe/C showed inferior catalytic activity at lower temperatures compared to the KH-based catalysts (Figure S22), confirming that the Fe^0 content alone cannot account for the delayed onset in catalytic activity. TPD results, as will be discussed in the next section, show that hydrogen release from LiH/Fe/C continues well into the isothermal hold of the heat treatment, and yet is incomplete, in contrast to KH and NaH. This demonstrates that the activation of LiH under the catalytic conditions is kinetically limited. Thus, if Li or Li-FeH_x is the catalytically active phase, it means that the active site is still evolving/being formed during the Arrhenius measurement, as seen from the catalytic data. This explains the high activation energy. Even when sufficient Li and Fe^0 (or Li-FeO_x) is formed, for instance, in the sample with 10 wt% LiH (Figure S18 and Table S3), the high stability of LiH (dehydrogenation enthalpy of 181.2 kJ/mol of H_2)[47] makes LiH the thermodynamically stable phase under the high hydrogen pressure (10 bar), hence a higher temperature is needed to shift the equilibrium to the Li + H_2 phase, where Li can interact more with Fe and N_2.

Upon cooling, LiH/Fe/C catalysts showed nearly identical catalytic activities and activation energies (Figure S23, Table S3). Therefore, the reduction of Fe_2O_3 during catalysis cannot account for the delayed onset in activity observed for the LiH/Fe/C catalysts at lower temperatures. This suggests that additional processes, beyond iron oxide reduction, especially the stability of the LiH and/or Li–Fe–H_x phases, influence ammonia synthesis in LiH/Fe/C under these conditions.

Even though the initial reduction treatment of the Fe_2O_3 nanoparticles (before adding the AHs) did not appear to significantly change the properties and/or composition of the Fe metal center, the catalytic activity of AH/Fe/C is almost halved if the prior reduction treatment is not performed (Figure S24). We attribute this to the presence of surface groups on the carbon, as indicated by the CO/CO_2 formation during TPR (Figure S2). If not removed by reductive treatment under hydrogen, these surface groups react with the alkali hydride, resulting in their oxidation. The importance of inert handling is highlighted when the catalysts are exposed to air overnight. The HERFD-XANES results show near full oxidation for all samples, for example, the LCF of NaH/Fe/C, a near full conversion to Fe^{3+} (Table S1, Figure S25), and the catalytic activity was reduced to a maximum of 0.2 mmol NH_3 g^{-1} h^{-1} at 400 °C and 10 bar (Figure S26).

The stability of the catalysts was evaluated by monitoring ammonia production over time using 100 mg of catalyst under conditions of SV = 36,000 mL g^{-1} h^{-1}, 300 °C, and 10 bar (Figure S27). KH/Fe/C exhibits a brief activation period during the first two hours on stream, after which the activity decreases slightly and gradually through 8 h; nevertheless, the catalyst retains considerable activity after 26 h, indicating reasonable medium-term stability. LiH/Fe/C displays a different activation profile, with activity increasing progressively during the initial hours before plateauing at 8 h. The activation under reaction conditions is similar to the observed catalytic activities during heating and cooling, and similar to KH/Fe/C, this catalyst retains good activity after 26 h. NaH/Fe/C shows a similar activation pattern compared to LiH/Fe/C, and both plateauing around an ammonia production rate of 2.8 mmol g^{-1} h^{-1}. The major difference lies in the time in which the plateau is achieved, which is already after one hour on stream. This could be attributed to the slow kinetics of in-situ reduction of iron oxide in LiH/Fe/C due to the sluggish hydrogen release kinetics of LiH, as observed in the TPD. The different activation profiles across the three alkali hydride systems suggest that the activation dynamics are governed by the identity (stability) of the alkali hydride.

It is important to note that air exposure oxidizes both the Fe and alkali hydride components in the nanocomposite. While the reduction of the resulting Fe_2O_3 might be possible under high temperature (above 500 °C) and high hydrogen pressure, regeneration of the formed alkali hydroxides and oxides back to the metallic or hydride phase requires even harsher conditions due to their thermodynamic stability. Moreover, the conditions required for Fe reduction, high temperature and reducing atmosphere, would result in methanation of the carbon supports, further affecting the support properties. Deactivation due to oxidation/air exposure should therefore be avoided, highlighting the need for inert handling, storage, and use.

5. RESULTS—MECHANISTIC INVESTIGATIONS

Ammonia synthesis on heterogeneous catalysts involves the adsorption and activation of both N_2 and H_2. Alkali hydrides can reversibly adsorb/desorb H_2 and also form N_xH_y species, such as in KNH_2 and $LiNH_2$. As hydrides are expected to actively participate in the hydrogenation of adsorbed nitrogen species, high regeneration of these sites under catalytic conditions (high hydrogen absorption/release kinetics) could improve the overall catalytic activity. Therefore, we investigated the effects of nanoconfinement and the presence of Fe_2O_3 on H_2 absorption and release on the alkali metal hydrides. The AH/Fe/C catalysts were (re)hydrogenated at 275 °C, 20 bar, 2 h (H_2-AH/Fe/C).

The hydrogen formation during the initial heat treatment and after (re)hydrogenation was compared in Table 2 and Figure 5. The nanocomposites showed peak hydrogen release at significantly lower temperatures than those reported for the bulk AHs; therefore, the presence of a porous carbon resulted in a large decrease in decomposition temperatures. The presence of Fe_2O_3 did not have a significant impact on the decomposition behavior nor the amount of hydrogen released (Table 2 and Figure S28), indicating that the improved decomposition behavior is primarily governed by the porous carbon support rather than interaction with Fe_2O_3. Thus, the presence

Table 2. Hydrogen Release Quantities (%H) of the Prepared Nanocomposites during TPD Measurements

sample composition	AH ref. (%H)	AH/C (%H)	AH/Fe/C (%H)	H_2-AH/Fe/C (%H)
LiH	3	48	55	25
NaH	97	77	77	66
KH	85	89	94	70

https://doi.org/10.1021/acscatal.6c02968
ACS Catal. XXXX, XXX, XXX–XXX

Downloaded from http://pubs.acs.org/accacs/article-pdf/doi/10.1021/acscatal.6c02968/66127963/cs-2026-029683.pdf by guest on 27 July 2026

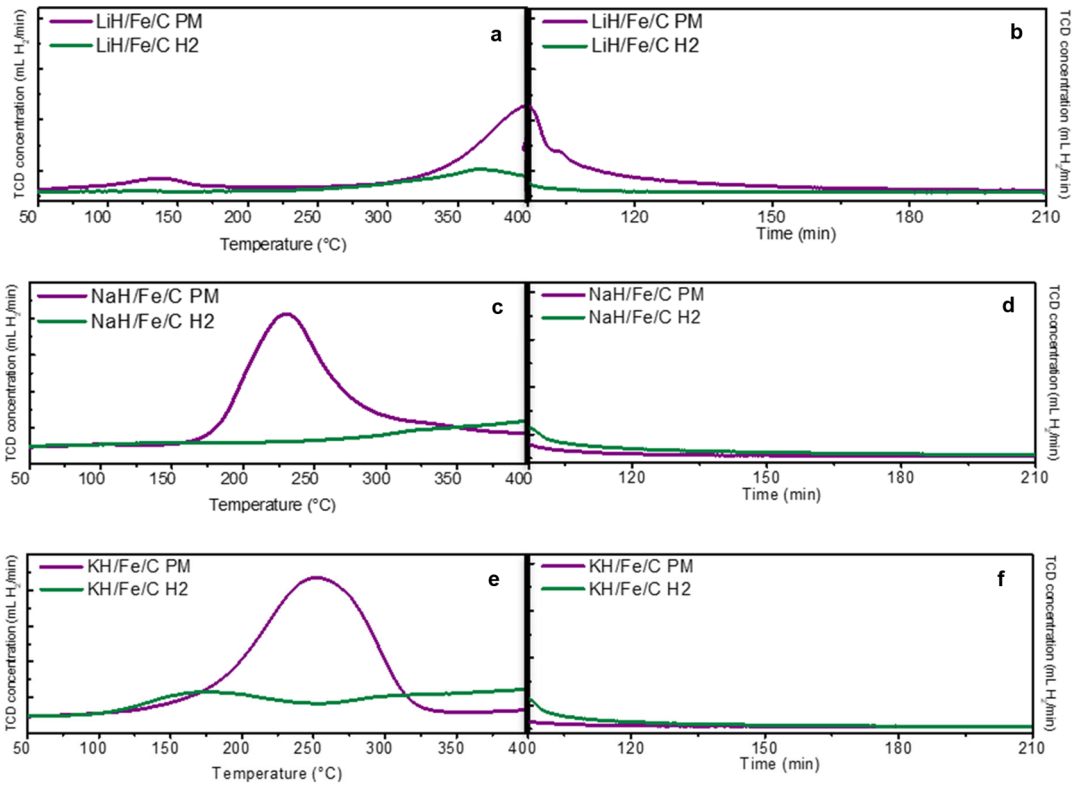

Figure 5. Temperature-programmed desorption profiles (Ar-TPD) of the physical mixtures of AH + C before heat treatment (PM) and hydrogen (H_2)-treated AH/Fe/C catalysts under a flow of argon during the heating step (5 °C min^{-1} to 400 °C) and the subsequent 2 h isothermal hold for LiH/Fe/C (a, b), NaH/Fe/C (c, d), and KH/Fe/C (e, f). The release of hydrogen indicated the partial decomposition of AH, either thermally or by the reaction with the porous graphite support.

of the graphitic carbon support leads to significant improvement in the thermal decomposition and reactivity of the hydrides.

After the first hydrogen release measurements (TPD), the decomposed samples were re-hydrogenated, and a second TPD was then conducted. Based on the second TPD, all the catalysts showed reversible hydrogen release/uptake (Table 2). A decrease in hydrogen release for the second cycle is often observed for metal hydrides in reversible hydrogen storage applications, especially for the nanocomposite materials.[48,49] This is often attributed to a more sluggish re-hydrogenation kinetics (especially under these experimental conditions) compared to dehydrogenation, and/or irreversible reaction with the carbon matrix (surface groups) to form inactive materials. Nevertheless, all catalyst compositions exhibited reversible hydrogen uptake and release under the conditions tested, which is relevant for their use in ammonia synthesis. The difference in their reversible capacity highlights the differences in the interaction of the AHs with the carbon and in their hydrogen absorption kinetics.

To study the N_2 activation and (de)hydrogenation of the different catalysts, the fresh catalysts were treated with 20 bar N_2 at 285 °C for 10 h. This treatment should lead to the adsorption/activation of N_2 and/or the formation of surface nitrides/amides. After this step, the samples were subjected to H_2-TPR and Ar-TPD (Figure 6). Temperature-programmed desorption under an argon atmosphere (Ar-TPD, Figure 6b,d) did not show release of N_2 or NH_3 from the LiH/Fe/C and NaH/Fe/C catalysts. Lithium amide is known to undergo a multi-step thermal decomposition, producing ammonia between 300 and 450 °C, whereas sodium amide decomposes between 200 and 400 °C, producing ammonia and hydrogen, neither of which was observed in the samples. However, N_2 was observed for KH/Fe/C at 250–400 °C (Figure 6f), which matches the decomposition temperature of KNH_2. Note that all three catalysts released H_2 at 250–425 °C, indicating that in the absence of hydrogen pressure, the alkali hydrides decompose further after melt infiltration.

To investigate the hydrogenation step, the nitrogen-treated catalysts were heated under a 5% H_2/Ar flow (Figure 6a,c,e). Only for potassium, N_2 and NH_3 were detected between 200 and 400 °C, most presumably originating from the hydrogenation of the surface nitrogen species. The onset of ammonia production overlaps with the lowest temperature at which ammonia is observed under reaction conditions. For sodium, a more pronounced ammonia peak is observed. The TPD and TPR results suggest that KH is better able to activate N_2; perhaps it has the most favorable intermediate binding strength with N, and hence can readily absorb and desorb N_2. This could also be related to its ability to form graphite intercalated KH (KH-GIC),[22] which has been shown to bind molecular N_2 under moderate conditions.

The Ar-TPD and H_2-TPR on the nitrogen-treated catalysts (N_2-KH/Fe/C and N_2-NaH/Fe/C) confirm that both catalysts are capable of activating N_2. However, the nature and strength of nitrogen binding are different between the two catalysts. N_2-KH/Fe/C released small amounts of N_2 under Ar flow and NH_3 under H_2 flow, indicating a relatively weak interaction

https://doi.org/10.1021/acscatal.6c02968
ACS Catal. XXXX, XXX, XXX−XXX

Downloaded from http://pubs.acs.org/accacs/article-pdf/doi/10.1021/acscatal.6c02968/66127963/cs-2026-029683.pdf by guest on 27 July 2026

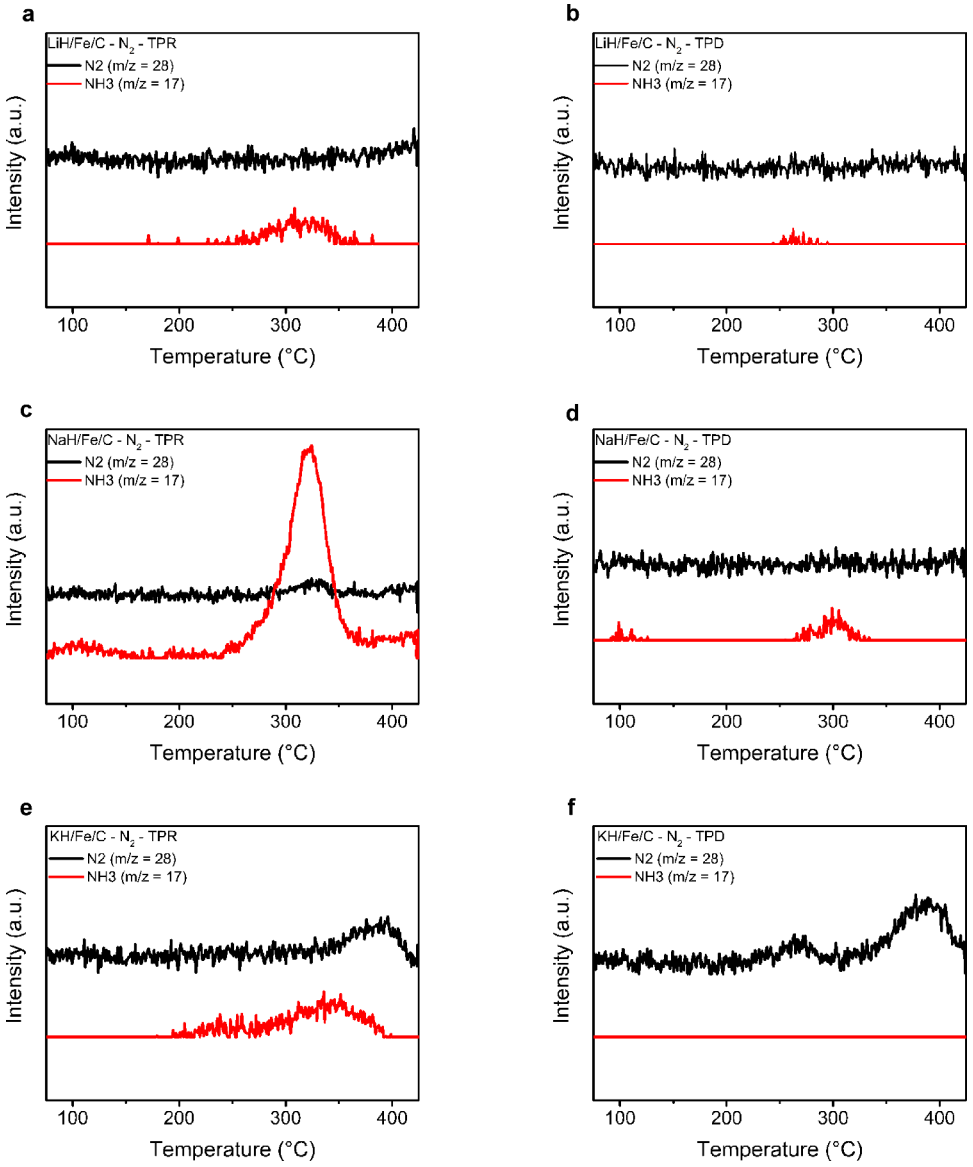

Figure 6. MS signals of N_2 ($m/z = 28$) and NH_3 ($m/z = 17$) during temperature-programmed reduction (H_2-TPR) and desorption (Ar-TPD) of the nitrogen-treated LiH/Fe/C (a, b), NaH/Fe/C (c, d), and KH/Fe/C (e, f) catalysts (70 mg). CH_4 ($m/z = 16$) was also monitored to check for support methanation, but none was observed under these conditions.

between the catalyst and nitrogen. On the other hand, N_2-NaH/Fe/C showed large amounts of NH_3 formation under a reducing atmosphere, but at a higher temperature, and no N_2 was released under an inert (Ar) atmosphere. These results indicate that adsorbed nitrogen is bound more strongly on the N_2-NaH/Fe/C and hence cannot be desorbed as molecular dinitrogen under these mild conditions, as in the case of N_2-KH/Fe/C, but can be hydrogenated to ammonia. While the larger H_2-TPR peak for N_2-NaH/Fe/C indicates the formation of higher amounts of NH_3 due to stronger activation of N_2, this relatively stronger binding does not result in greater catalytic activity than for N_2-KH/Fe/C under the experimental conditions. This is also evident from the higher NH_3 release temperature observed for the N_2-NaH/Fe/C. These results are consistent with the Sabatier principle, where an intermediate binding strength is desired. The trend also follows the stability trend of the alkali metal amides and nitrides, which are considered possible intermediate species in AH-mediated ammonia synthesis. However, it is important to note that the TPD and TPR experiments were conducted under atmospheric pressure and gas flows dissimilar to the ammonia synthesis conditions, and therefore simply serve as mechanistic probes. As LiH/Fe/C was activated during ammonia synthesis, we also tested the spent LiH/Fe/C catalyst. After catalysis, the LiH/Fe/C catalyst was subjected to the same N_2-treatment, followed by H_2-TPR, and again, no significant formation of N_2 and/or NH_3 was observed (Figure S29).

The TPD/R results on Fe_2O_3/C showed that it is capable of nitrogen adsorption and/or activation, which is later released as N_2 under both Ar and H_2/Ar atmosphere (Figure S30). During catalytic testing, Fe_2O_3/C produced ammonia only at 400 °C, but in an amount that is 102 times lower than for the KH-promoted catalysts (Figure S19, 400 °C, 10 bar, 14.00 vs. 0.14 mmol g^{-1} h^{-1}). Note that this graphite support contains

https://doi.org/10.1021/acscatal.6c02968
ACS Catal. XXXX, XXX, XXX−XXX

Downloaded from http://pubs.acs.org/accacs/article-pdf/doi/10.1021/acscatal.6c02968/66127963/cs-2026-029683.pdf by guest on 27 July 2026

~0.13 at% of N due to nitrogen-containing groups, as commonly found on graphitic porous carbon materials.[31]

For the Fe/C, KH-, and LiH-based catalysts, the H_2 and N_2 treatments had minor effects on the Fe K-edge HERFD-XANES spectra when compared to the fresh catalysts (Figures S12, S31, and S32). This is in line with the observed weak interaction between H_2/N_2 and the catalysts. However, the NaH/Fe/C catalysts proved to be much more sensitive to these treatments (Figure S33). The N_2-NaH/Fe/C showed a significant increase in %Fe^0, from 25 to 62% (Table S1). The H_2-NaH/Fe/C pre-edge peak splitting in Figure S33 revealed that the iron coordination had changed to octahedral Fe, compared to the tetrahedral Fe observed for Fe/C. We attribute this to the reversible formation of sodium ferrite, which has been reported to result in variations in Fe-O bond length and Fe coordination,[50] combined with the peak at 7138 eV, which only appeared for the NaH/Fe/C samples. The specific peak at 7138 eV has been observed after annealing stainless steel at 900 °C under N_2[51] and in Fe-containing perovskites,[52] but without a clear designation or any of the other characteristic features observed for NaH/Fe/C. This proves that the interaction between Fe and Na is much stronger, although this does not lead to additional benefits in ammonia synthesis, compared to the other AH/Fe/C.

The catalytic activity trend KH > NaH > LiH under these mild reaction conditions can be explained by the electron-donating ability and stability/reactivity of the hydride phase. Alkali hydrides act as electron donors to the adjacent iron species, which is expected to improve both the reduction of Fe_2O_3, as well as promote the N_2 activation through increased back-donation. The enhanced reduction of Fe_2O_3 is confirmed by the XANES and LCF results, which indicate that the concentration of the Fe^0 follows the same trend in the fresh AH/Fe/C catalysts. KH is the least stable or most reactive among the three hydrides, and the highest electron donor. It is also known to react readily with graphitic carbon, leading to destabilization and sometimes intercalation of K-ion, and thereby hydrogen release under moderate conditions. Clearly, the TPD data show that the KH-based nanocomposite has the lowest hydrogen release temperature. Additionally, the XRD results confirm the interaction between KH and the carbon to form an intercalated phase (KH-GIC), which presumably influences the electronic environment, facilitates the interaction with, and reduction of, the FeO_x phase.

KH is closely followed by NaH in terms of stability and electron donation, while LiH is quite stable, showing sluggish hydrogen release kinetics, and thereby low interaction with FeO_x as explained above. These observations are also remarkably in accordance with the trend observed for alkali (hydr)oxide, imides, or amide promoters,[53] where the activity trend is shown to follow the electron-donating strength trend, K > Na > Li. Therefore, we propose that catalysis occurs at the interface between the reduced iron nanoparticles and the alkali metal, where both nitrogen activation and hydrogenation can occur in close proximity. However, a full identification of the interfacial active sites requires dedicated characterization beyond the scope of this work.

6. CONCLUSIONS

We have investigated the catalytic activity of alkali metal hydrides and iron oxide nanoparticles co-confined in graphitic carbon nanoscaffolds. By combining incipient wetness impregnation and melt infiltration, we prepared AH/Fe_yO_x/C nanocomposites (AH = LiH, NaH, and KH, 4.17 mmol AH g_{cat}^{-1}). These catalysts exhibit impressive catalytic activity for ammonia synthesis under mild conditions, even without complete reduction of the iron oxide. The catalytic activities of these AH/Fe/C nanocomposites surpassed that of the unpromoted classical Ru/MgO catalyst under identical reaction conditions. Results from structural and electronic characterizations suggest that the high catalytic activity is due to the intimate contact between the AH, Fe_2O_3 nanoparticles, and the graphitic carbon. This facilitates the reduction of Fe-O to catalytically active Fe^0, promotes N_2 activation on the catalysts, and enhances the kinetics of hydrogen sorption on the alkali hydrides, thereby facilitating hydrogenation of the nitrogen intermediates to NH_3.

The catalytic activity of the nanocomposites is highly dependent on the AHs, with KH/Fe/C > LiH/Fe/C > NaH/Fe/C > Fe/C. Remarkably, the LiH-based samples show a composition-dependent activation, unlike the other catalysts. These distinctions are related to differences in the interaction of the nano-confined AH with Fe_2O_3 nanoparticles, as well as with N_2 and H_2. These results demonstrate that the addition of alkali metal hydrides is a promising approach to develop novel ammonia synthesis catalysts that are active under milder conditions (temperature and pressure), even when transition metal oxides are used instead of the fully reduced metal phase.

■ ASSOCIATED CONTENT

Supporting Information

The Supporting Information is available free of charge at https://pubs.acs.org/doi/10.1021/acscatal.6c02968.

Characterization data: TPR-MS, STEM-EDX, HERFD-XANES, LCF, XRD, TPD, TPD-MS; catalytic performance data; and supplementary figures and tables (DOCX)

■ AUTHOR INFORMATION

Corresponding Author

Peter Ngene – *Materials Chemistry and Catalysis, Debye Institute for Nanomaterials Science, Universiteit Utrecht, Universiteitsweg 99, 3584 CG Utrecht, The Netherlands*; orcid.org/0000-0003-3691-0623; Email: p.ngene@uu.nl

Authors

Juliette C. Verschoor – *Materials Chemistry and Catalysis, Debye Institute for Nanomaterials Science, Universiteit Utrecht, Universiteitsweg 99, 3584 CG Utrecht, The Netherlands*; orcid.org/0000-0002-9204-6203

Fabian J. Mohammad – *Materials Chemistry and Catalysis, Debye Institute for Nanomaterials Science, Universiteit Utrecht, Universiteitsweg 99, 3584 CG Utrecht, The Netherlands*

Masoud Lazemi – *Materials Chemistry and Catalysis, Debye Institute for Nanomaterials Science, Universiteit Utrecht, Universiteitsweg 99, 3584 CG Utrecht, The Netherlands*; orcid.org/0000-0003-0118-7113

Shusaku Hayama – *Diamond Light Source Ltd, Harwell Science and Innovation Campus, Didcot, Oxfordshire OX11 0DE, U.K.*

Downloaded from http://pubs.acs.org/accacs/article-pdf/doi/10.1021/acscatal.6c02968/66127963/cs-2026-029683.pdf by guest on 27 July 2026

Nitya Ramanan – *Diamond Light Source Ltd, Harwell Science and Innovation Campus, Didcot, Oxfordshire OX11 0DE, U.K.*

Frank M. F. de Groot – *Materials Chemistry and Catalysis, Debye Institute for Nanomaterials Science, Universiteit Utrecht, Universiteitsweg 99, 3584 CG Utrecht, The Netherlands*

Petra E. de Jongh – *Materials Chemistry and Catalysis, Debye Institute for Nanomaterials Science, Universiteit Utrecht, Universiteitsweg 99, 3584 CG Utrecht, The Netherlands; Materials Chemistry and Catalysis, Institute for Sustainable and Circular Chemistry, Universiteit Utrecht, Universiteitsweg 99, 3584 CG Utrecht, The Netherlands*

Complete contact information is available at:
https://pubs.acs.org/doi/10.1021/acscatal.6c02968

Notes

The authors declare no competing financial interest.

■ ACKNOWLEDGMENTS

Erik Betz-Güttner is acknowledged for the HAADF-STEM measurements. Robert Scott is thanked for providing the iron reference dataset. J.C.V., F.J.M., M.L., and P.N. are grateful to Diamond Light Source for providing the beamtime (Proposal ID: SP39324-1) and financial support for performing experiments at the I20-scanning beamline. F.J.M., M.L., and P.N. received funding from the ERC Consolidator grant 101171583. The HERFD-XANES data presented in this work are part of a larger dataset, which was obtained using both the ID26 beamline at the European Synchrotron Radiation Facility (ESRF) and the I-20 beamline at Diamond Light Source (DLS). The authors thank Jan Pieter Glatzel, Vasyl Marchuk, and Pranav Kulkarni for their assistance at ID26. This work was funded by the European Union under grant agreement 101058565 (AMBHER). Views and opinions expressed are, however, those of the author(s) only and do not necessarily reflect those of the European Union or European Health and Digital Executive Agency. Neither the European Union nor the granting authority can be held responsible for them.

■ REFERENCES

(1) Faria, J. A. Renaissance of ammonia synthesis for sustainable production of energy and fertilizers. *Curr. Opin. Green Sustainable Chem.* **2021**, *29*, 100466.

(2) Humphreys, J.; Lan, R.; Tao, S. Development and Recent Progress on Ammonia Synthesis Catalysts for Haber–Bosch Process. *Adv. Energy Sustainability Res.* **2021**, *2*, 2000043.

(3) Guo, J.; Chen, P. Catalyst: NH_3 as an Energy Carrier. *Chem* **2017**, *3*, 709–712.

(4) Tawalbeh, M.; et al. Ammonia: A versatile candidate for the use in energy storage systems. *Renewable Energy* **2022**, *194*, 955–977.

(5) Aziz, M.; TriWijayanta, A.; Nandiyanto, A. B. D. Ammonia as effective hydrogen storage: A review on production, storage and utilization. *Energies* **2020**, *13*, 3062.

(6) Chang, F.; et al. Influence of alkali metal amides on the catalytic activity of manganese nitride for ammonia decomposition. *Catal. Today* **2017**, *286*, 141–146.

(7) Wang, Q.; Guo, J.; Chen, P. Recent progress towards mild-condition ammonia synthesis. *J. Energy Chem.* **2019**, *36*, 25–36.

(8) Guo, J.; et al. Highly active MnN-Li_2NH composite catalyst for producing CO_x-free hydrogen. *ACS Catal.* **2015**, *5*, 2708–2713.

(9) Al Maksoud, W.; et al. Active and stable Fe-based catalyst, mechanism, and key role of alkali promoters in ammonia synthesis. *J. Catal.* **2021**, *394*, 353–365.

(10) Zincir, B. Environmental and economic evaluation of ammonia as a fuel for short-sea shipping: A case study. *Int. J. Hydrogen Energy* **2022**, *47*, 18148–18168.

(11) Ravi, M.; Makepeace, J. W. Facilitating green ammonia manufacture under milder conditions: What do heterogeneous catalyst formulations have to offer?. *Chem. Sci.* **2022**, *13*, 890–908.

(12) Logadottir, A.; et al. The Brønsted-Evans-Polanyi relation and the volcano plot for ammonia synthesis over transition metal catalysts. *J. Catal.* **2001**, *197*, 229–231.

(13) Aika, K. i. Role of alkali promoter in ammonia synthesis over ruthenium catalysts—Effect on reaction mechanism. *Catal. Today* **2017**, *286*, 14–20.

(14) Kowalczyk, Z.; Sentek, J.; Jodzis, S.; Muhler, M.; Hinrichsen, O. Effect of potassium on the kinetics of ammonia synthesis and decomposition over fused iron catalyst at atmospheric pressure. *J. Catal.* **1997**, *169*, 407–414.

(15) Paál, Z.; Ertl, G.; Lee, S. B. Interactions of potassium, oxygen and nitrogen with polycrystalline iron surfaces. *Appl. Surf. Sci.* **1981**, *8*, 231–249.

(16) Kitano, M.; et al. Electride support boosts nitrogen dissociation over ruthenium catalyst and shifts the bottleneck in ammonia synthesis. *Nat. Commun.* **2015**, *6*, 6731–6739.

(17) Kitano, M.; et al. Ammonia synthesis using a stable electride as an electron donor and reversible hydrogen store. *Nat. Chem.* **2012**, *4*, 934–940.

(18) Hosono, H. Electride Catalysts for Ammonia Synthesis. In *CO_2 Free Ammonia as an Energy Carrier*; Taylor and Francis, **2022**; pp 325–338.

(19) Medford, A. J.; et al. From the Sabatier principle to a predictive theory of transition-metal heterogeneous catalysis. *J. Catal.* **2015**, *328*, 36–42.

(20) Chang, F.; et al. Alkali and Alkaline Earth Hydrides-Driven N_2 Activation and Transformation over Mn Nitride Catalyst. *J. Am. Chem. Soc.* **2018**, *140*, 14799–14806.

(21) Hattori, M.; Miyashita, K.; Nagasawa, Y.; Suzuki, R.; Hara, M. Ammonia Synthesis Over an Iron Catalyst with an Inverse Structure. *Adv. Sci.* **2025**, *12*, 2410313.

(22) Chang, F.; et al. Potassium hydride-intercalated graphite as an efficient heterogeneous catalyst for ammonia synthesis. *Nat. Catal.* **2022**, *5*, 222–230.

(23) Gao, W.; et al. Barium Hydride-Mediated Nitrogen Transfer and Hydrogenation for Ammonia Synthesis: A Case Study of Cobalt. *ACS Catal.* **2017**, *7*, 3654–3661.

(24) Wang, P.; et al. Breaking scaling relations to achieve low-temperature ammonia synthesis through LiH-mediated nitrogen transfer and hydrogenation. *Nat. Chem.* **2017**, *9*, 64–70.

(25) Bramwell, P. L.; Ngene, P.; de Jongh, P. E. Carbon supported lithium hydride nanoparticles: Impact of preparation conditions on particle size and hydrogen sorption. *Int. J. Hydrogen Energy* **2017**, *42*, 5188–5198.

(26) Chen, Z.; et al. Iron-Single Sites Confined by Graphene Lattice for Ammonia Synthesis under Mild Conditions. *ACS Catal.* **2023**, *13*, 14385–14394.

(27) Spencer, N. D.; Schoonmaker, R. C.; Somorjai, G. A. Iron single crystals as ammonia synthesis catalysts: Effect of surface structure on catalyst activity. *J. Catal.* **1982**, *74*, 129–135.

(28) Hattori, M.; Okuyama, N.; Kurosawa, H.; Hara, M. Low-Temperature Ammonia Synthesis on Iron Catalyst with an Electron Donor. *J. Am. Chem. Soc.* **2023**, *145*, 7888–7897.

(29) Dahl, P. J.; et al. *New SynCOR Ammonia TM process*, **2017**. https://info.topsoe.com/new-syncor-ammonia-process-wp-dlp (accessed Jan 22, 2026).

(30) Sehested, J.; Jacobsen, C. J. H.; Törnqvist, E.; Rokni, S.; Stoltze, P. Ammonia synthesis over a multipromoted iron catalyst: Extended set of activity measurements, microkinetic model, and hydrogen inhibition. *J. Catal.* **1999**, *188*, 83–89.

Downloaded from http://pubs.acs.org/accacs/article-pdf/doi/10.1021/acscatal.6c02968/66127963/cs-2026-029683.pdf by guest on 27 July 2026

(31) Mattarozzi, F.; et al. Surface-Modified Carbon Materials for CO_2 Electroreduction. *Eur. J. Inorg. Chem.* **2023**, *26*, e202300152.
(32) Visser, N. L.; et al. Influence of carbon support surface modification on the performance of nickel catalysts in carbon dioxide hydrogenation. *Catal. Today* **2023**, *418*, 114071.
(33) Hayama, S.; et al. Fourteen-analyser high-resolution hard X-ray emission spectrometer at I20 beamline at Diamond Light Source. *J. Synchrotron Radiat.* **2026**, *33*, 848.
(34) Aramini, M.; Arrigo, R. Carbon surface chemistry drives speciation and reactivity of cationic Fe species in CO_2 activation: a HERFD-XANES and valence-to-core XES study. *Catal. Sci. Technol.* **2025**, *15*, 5046–5054.
(35) Lais, T.; et al. Elucidation of copper environment in a Cu-Cr-Fe oxide catalyst through in situ high-resolution XANES investigation. *Phys. Chem. Chem. Phys.* **2021**, *23*, 5888–5896.
(36) Boubnov, A.; et al. Selective catalytic reduction of no over fe-zsm-5: Mechanistic insights by operando herfd-xanes and valence-to-core xray emission spectroscopy. *J. Am. Chem. Soc.* **2014**, *136*, 13006–13015.
(37) Agote-Arán, M.; et al. Operando HERFD-XANES/XES studies reveal differences in the activity of Fe-species in MFI and CHA structures for the standard selective catalytic reduction of NO with NH_3. *Appl. Catal. A Gen.* **2019**, *570*, 283–291.
(38) Ravel, B.; Newville, M. ATHENA, ARTEMIS, HEPHAESTUS: Data analysis for X-ray absorption spectroscopy using IFEFFIT. *J. Synchrotron Radiat.* **2005**, *12*, 537–541.
(39) Yao, Y.; Hu, Y.; Scott, R. W. J. Watching iron nanoparticles rust: An in situ x-ray absorption spectroscopic study. *J. Phys. Chem. C* **2014**, *118*, 22317–22324.
(40) Bramwell, P. L.; et al. A transition-metal-free hydrogenation catalyst: Pore-confined sodium alanate for the hydrogenation of alkynes and alkenes. *J. Catal.* **2016**, *344*, 129–135.
(41) Adelhelm, P.; De Jong, K. P.; De Jongh, P. E. How intimate contact with nanoporous carbon benefits the reversible hydrogen desorption from NaH and $NaAlH_4$. *Chem. Commun.* **2009**, 6261–6263.
(42) De Jongh, P. E.; Adelhelm, P. Nanosizing and nanoconfinement: New strategies towards meeting hydrogen storage goals. *ChemSusChem* **2010**, *3*, 1332–1348.
(43) Imai, H.; et al. In situ and real-time monitoring of oxide growth in a few monolayers at surfaces of platinum nanoparticles in aqueous media. *J. Am. Chem. Soc.* **2009**, *131*, 6293–6300.
(44) Sun, Y. P.; Li, X. q.; Cao, J.; Zhang, W. x.; Wang, H. P. Characterization of zero-valent iron nanoparticles. *Adv. Colloid Interface Sci.* **2006**, *120*, 47–56.
(45) Reinsch, B. C.; Forsberg, B.; Penn, R. L.; Kim, C. S.; Lowry, G. V. Chemical transformations during aging of zerovalent iron nanoparticles in the presence of common groundwater dissolved constituents. *Environ. Sci. Technol.* **2010**, *44*, 3455–3461.
(46) Wang, P.; et al. The Formation of Surface Lithium–Iron Ternary Hydride and its Function on Catalytic Ammonia Synthesis at Low Temperatures. *Angew. Chem., Int. Ed.* **2017**, *129*, 8842–8846.
(47) Abbas, M. A.; Grant, D. M.; Brunelli, M.; Hansen, T. C.; Walker, G. S. Reducing the dehydrogenation temperature of lithium hydride through alloying with germanium. *Phys. Chem. Chem. Phys.* **2013**, *15*, 12139–12146.
(48) Ichikawa, T.; Fujii, H.; Isobe, S.; Nabeta, K. Rechargeable hydrogen storage in nanostructured mixtures of hydrogenated carbon and lithium hydride. *Appl. Phys. Lett.* **2005**, *86*, 241914, .
(49) Gao, J.; et al. Enhanced reversibility of H 2 sorption in nanoconfined complex metal hydrides by alkali metal addition. *J. Mater. Chem.* **2012**, *22*, 13209–13215.
(50) Takeda, Y.; et al. Sodium deintercalation from sodium iron oxide. *Mater. Res. Bull.* **1994**, *29*, 659–666.
(51) Lützenkirchen-Hecht, D.; et al. Thermal anti-oxidation treatment of CrNi-steels as studied by EXAFS in reflection mode: The influence of monosilane additions in the gas atmosphere of a continuous annealing furnace. *J. Mater. Sci.* **2014**, *49*, 5454–5461.
(52) Luongo, G. *Chemical Looping for Process Efficiency Enhancement*; ETH Zurich, **2023**.
(53) Gao, W.; Guo, J.; Chen, P. Hydrides, Amides and Imides Mediated Ammonia Synthesis and Decomposition. *Chin. J. Chem.* **2019**, *37*, 442–451.

Downloaded from http://pubs.acs.org/accacs/article-pdf/doi/10.1021/acscatal.6c02968/66127963/cs-2026-029683.pdf by guest on 27 July 2026

https://doi.org/10.1021/acscatal.6c02968
ACS Catal. XXXX, XXX, XXX–XXX